www.czasopisma.pan.pl PAN www.journals.pan.pl

ARCHIVES of FOUNDRY ENGINEERING

ISSN (2299-2944)
Volume 2023
Issue 3/2023

38 – 50

10.24425/afe.2023.146661

6/3

Published quarterly as the organ of the Foundry Commission of the Polish Academy of Sciences

Simulation and Heat Treatment Process of Carbon Nanotube Modified Aluminum Alloy (ZL105)

Ziqi Zhang [a], Zhilin Pan [a], Rong Li [a,*], Qi Zeng [b], Yong Liu [c], Quan Wu [a]

[a] School of Mechanical & Electrical Engineering, Guizhou Normal University, China
[b] Guiyang Huaheng Mechanical Manufacture CO.,LTD, China
[c] Guizhou University, China
*Corresponding author E-mail address: lirong9242001@163.com

Received 10.10.2022; accepted in revised form 11.03.2023; available online 02.08.2023

Abstract

To further improve the mechanical properties of carbon nanotubes (CNTs) modified aluminum alloy (ZL105), the first principle was used to build the atomic structure of the alloy system and the alloy system was simulated by the VASP. After that, the heat treatment process of the cast aluminium alloy material with CNTs to enhance the alloy performance by the orthogonal experiment. The results of the research show that: (1) The energy status of the alloy system could be changed by adding the C atoms, but it did not affect the formation and structural stability of the alloy system, and the strong bond compounds formed by C atoms with other elements inside the solid solution structure can significantly affect the material properties. (2) The time of solid solution has the greatest influence on the performance of material that was modified by CNTs. The solution temperature and aging temperature were lower strength affection, and the aging time is the lowest affection. This paper provides a new research method of combining the atomic simulation with the casting experiment, which can provide the theoretical calculations to reduce the experiment times for the casting materials' performance improvement.

Keywords: Cast aluminum alloy, Heat treatment, CNTs; First principle, Mechanical performance

1. Introduction

Aluminum alloys have been widely used in the manufacture of many auto parts, and aluminum matrix composites with good performance can be prepared by using particle-reinforced or fiber-reinforced aluminum alloys [1-4]. Existing alloy properties are mainly improved by adding reinforcement to improve the internal microstructure and structure of the material. For example, the author's team used the casting method to add fibrous carbon nanotubes as reinforcement to aluminum alloy (ZL105), which significantly improved the mechanical properties of the aluminum alloy. At the same time, many studies have shown that the optimization of the heat treatment process parameters of metal materials can also effectively improve the mechanical properties of the materials [5, 6]. According to the existing research situation, the enhancement mechanism of aluminum alloy is mainly to improve the performance of the composite material by changing the interface bonding mode of the composite material or changing the internal microstructure and distribution state [7, 8].

In practical applications, the properties of alloy materials are greatly affected by their casting and heat treatment processes. The changed process of the performance of alloy materials obtained by experiments was very complex, and the directivity was not clear. An accurate prediction is impossible for new material. With the development of computational materials science, the construction

of an alloy atoms system was made and simulated by calculating software. So the energy state and electronic structure between atoms are calculated, and the evolution of the internal microstructure of alloy materials after heat treatment was also discussed. Atomic-level simulation studies of alloy heat treatment were explored during the various physical and chemical reactions that occurred in the alloy heat treatment process, and then the mechanism of the materials' properties changed also discussed. S.H. Zhou et al. [9-11] used first-principles methods combined with heat treatment experiments to calculate the stability range and relative stability of intermetallic phases in the alloy system, as well as the various phase components produced by heat treatment. Lukas Stemper et al. [12-14] calculated the different steps of the heat treatment experiment through atomic-level simulation, the characteristics of the microstructure formation of materials were studied during the heat treatment process and obtained the optimal heat treatment process conditions of the alloy. Deni Haryadi et al. [15, 16] traced the reasons for better mechanical properties of alloys obtained in heat treatment experiments at the atomic level by simulating the interfacial and strain energy of precipitated phases of heat treated materials. With the evolution of computing technology, alloy atomic level simulation can be used for theoretical calculations to improve various problems such as defect formation and mechanical damage in practical applications of materials through the heat treatment process [17, 18]. At the same time, the James equation of the heat conversion of the alloy during the heat treatment process and the quantum mechanical mechanism of different reactions such as grain formation can be further studied and captured, which can design alloy materials with excellent performance [19, 20].

Based on the previously prepared carbon nanotube-reinforced cast aluminum alloy (ZL105) composite, this paper calculates the electronic properties of the composite, including band structure, state density, and charge density, using first principles, to analyze the influence of carbon atom doping on the mechanical properties of the material. After that, the main parameters in the heat treatment process parameters of carbon nanotube-modified aluminum alloy were studied by the orthogonal experiment method, and it was expected to obtain the best heat treatment process parameters of this composite material and effectively improve the alloy properties.

2. Simulation and Experiment

2.1. Simulation Calculation

2.1.1. Modeling

The crystal cell model of aluminum-based composite materials was used to build aluminum composite materials by Materials Studio software as shown in Fig. 1. The space group is P1, Lattice constant: a=10.41370 Å, b=3.97973 Å, c=10.46858 Å; α = 90.0000°, β =119.4654°, γ = 90.0000°; V = 377.7389 Å$^{\wedge 3}$. To compare the performance of the material with carbon nanotubes, the carbon atoms are mixed in this crystal cell to get the crystal cell model as shown in Fig. 2, and the two crystal cells will be simulated at the same time.

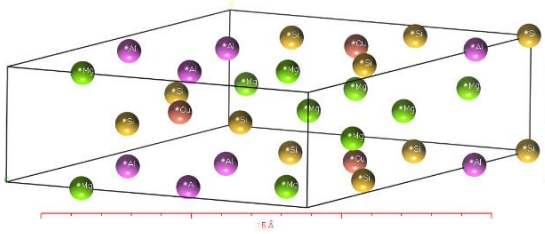

Fig. 1. Crystal cell model of aluminium alloy

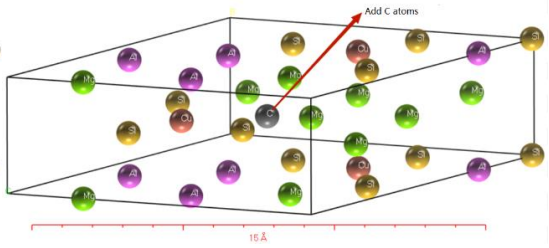

Fig. 2. Crystal cell model containing carbon atoms

2.1.2. Simulation parameter settings

In this experimental simulation calculation, the VASP software package (Vienna ab initio simulation package) was used to calculate the electronic properties of the alloy system [21, 22]. To calculate the valence electrons while ignoring the influence between electrons in the core layer, the projected subadditive wave (PAW) method was used to accurately describe the interaction between electrons and ions, the exchange-correlation function between electrons was treated by the PBE functional under the generalized gradient approximation (GGA) [23, 24]. The valence electron configuration of each atom is Mg-3s^2, Al-3s^{2}3p^1, Cu-3d^{10}4s^1, Si-3s^{2}3p^2, and C-s^{2}p^2. The electron Kohn-Sham wave function of the system was expanded by the plane wave basis set, The k-point of the parsimonious Brillouin zone of the crystal cell model uses the Gamma point as the center to generate a grid [25]. After the convergence testing, the grid numbers of the crystal cells were 5×13×5 and 6×13×6 respectively, the plane wave truncation energy was 450eV, and the convergence criterion of the self-consistent cycle (SCF) calculation was set to 1×10^{-5} eV/atom, the force convergence criterion was -0.01 eV/nm [26], and set the calculation accuracy to the highest (PREC=Accurate) for structural optimization. After optimization, non-self-consistent calculations were performed to obtain the band structure, density of states, and charge density of the system, The Vaspkit program [27] was used to extract data to visualize the calculation results.

2.2. Experiment

2.2.1. Material formula

ZL105 aluminum alloy material was smelted by itself according to the national standard formula (GB/T 1173-1995), and its specific components and contents are shown in Table 1.

Table 1.
ZL105 Alloy composition and content (Content: %)

Element	Al	Cu	Si	Mg
Content	92.9(Double Zero Aluminum)	1.3	5.2	0.6

2.2.2. Experimental materials

The experimental composite material was made by smelting and casting, and its material components (mass fraction, %) were 1.3Cu, 5.2Si, and 0.6Mg, the remainder was Al. On this basis, a multi-walled carbon nanotube reinforcement material with a mass fraction of 1.25% was added. The above-mentioned component materials were smelted and poured into the mold, and the mold was opened to intercept the experimental materials shown in Fig. 3.

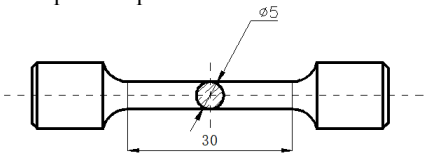

Fig. 3. Shape and size of composite test specimens

2.2.3. Experimental design method and experimental process

To determine the optimal heat treatment process parameters of the material, the influence of the solution temperature, solution time, aging temperature, and aging time on the mechanical properties of the experimental materials was studied in the heat treatment parameters. Refer to the T5 heat treatment process parameters to set the numerical value of the factor level of this orthogonal experiment. Using SPSS25.0 software, select L9 (34) orthogonal table in this environment, the factor level table automatically generated by the system is shown in Table 2. At the same time, to reduce the error caused by the experimental design and improve the accuracy of the experimental results, three groups of repeated experiments were carried out according to the heat treatment scheme.

Table 2.
Orthogonal experiment factor level table

Factor / Level	A- Solution temperature /°C	B- Solution time /h	C- Aging temperature /°C	D- Aging time /h
Level 1	A_1=515	B_1=2	C_1=170	D_1=2
Level 2	A_2=525	B_2=4	C_2=180	D_2=4
Level 3	A_3=535	B_3=6	C_3=190	D_3=6

The heat treatment of each group of test materials was carried out successively according to the heat treatment scheme of the orthogonal table generated by the software. First, set the temperature of the experimental heat treatment furnace, and put the prepared composite material into the furnace for solution treatment. Secondly, after reaching the set solution time, the experimental material was put into 80°C water for quenching. Next, set the furnace temperature, and put the experimental materials into the heat treatment furnace for aging treatment. Finally, after reaching the set aging time, take it out and cool it at room temperature to prepare for the next mechanical property test.

2.2.4. Testing equipment

The strength of the experimental material was tested by a microcomputer servo-controlled hydraulic universal testing machine (WAW-300). The hardness was tested with an electric Blovi hardness tester (HBRV-187.5). The elongation was tested with an extensometer (YYU-5/25). The morphology of the metallographic structure was collected by a metallographic microscope (4XC-MS). The fracture morphology was collected by scanning electron microscope (SU8010). The internal structure was collected by transmission electron microscope (Tecnai G2).

3. Simulation and Experimental Results

3.1. Electronic Structure

The electronic properties of the system can be obtained through the calculation of VASP simulation software. Fig. 4 showed the constructed crystal cell electronic structure. Fig. 5 showed the electronic structure of a doped carbon nanotube crystal cell. And Fig. 6 showed the charge density of the constructed crystal cell. The Fermi level (E_f) in the figure is 0 eV, indicated by the red dashed line.

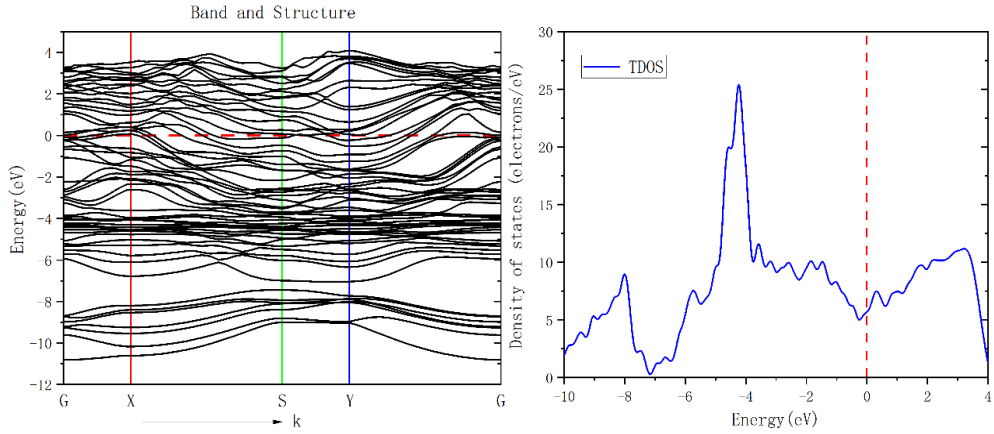

(a) Band structure and Total density of states (TDOS)

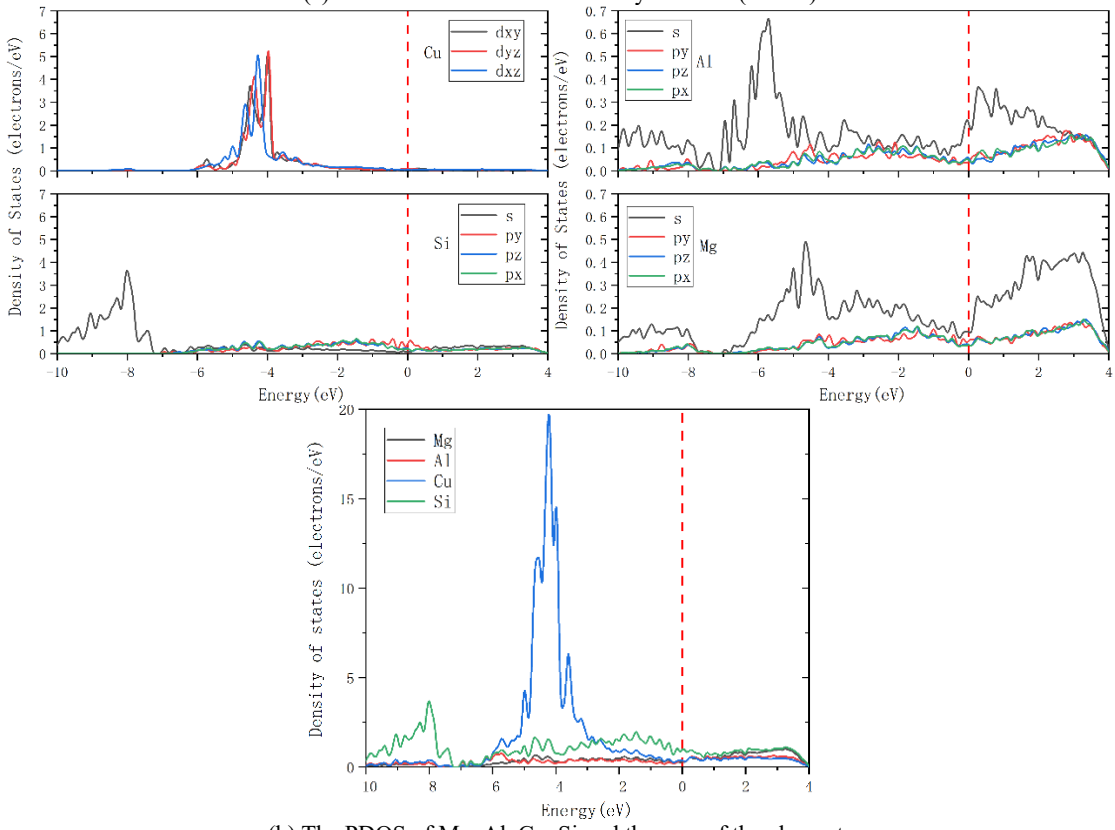

(b) The PDOS of Mg, Al, Cu, Si and the sum of the elements

Fig. 4. Build the electronic structure of the model

In the band structure diagram of Fig. 4-a, it can be seen first that the conduction band intersects with the Fermi level and passes through the Fermi level, and electrons can easily transition to the conduction band at room temperature. At the same time, we can also see that the DOS value across the Fermi surface is not zero in the total density of states, which proves that the material of this system is metal and has good conductivity. Secondly, the energy band is dense between -11eV and 5eV, the bandwidth is larger, the effective electron mass in the band is smaller, and the degree of non-localization of free electrons is larger. At this time, the outer electron orbitals of the nucleus have a strong expansion, which makes the adjacent orbitals overlap [28].

Observing the total state density map (TDOS) in Fig. 4-a, it can be found that a sharp peak appears at -4.5eV. The fluctuation of the energy level here in the energy band diagram is small, and the distribution is relatively even in the entire energy range, showing a smooth curve. Combined with the PDOS of Cu atoms in Fig. 4-b, the localized peak DOS here corresponds to the *d*-state valence electron contribution of Cu. The DOS values of Cu and Si are found to be far away from the Fermi level in the partial density of states,

which means that there is no hybrid orbital formed between Cu and Si, but an ionic bond compound is formed [29]. However, the bonding peak at -7.2 eV becomes smaller, the density of states of electrons is close to zero, and the corresponding energy band has no energy level intersection. It shows that there is a vacancy peak near the energy level here, and the peak of the metal bond is formed between the elements [30], which makes it easier to form a solid solution rather than a single intermetallic compound.

The energy distribution state plays an important role in the material properties, because it determines the state of the system or the properties and properties of the material, and the density of states corresponds to the energy distribution [31, 32]. In Fig. 4-b, the composition of the partial density of states of each atom can be observed, and the conduction band above the Fermi surface was mainly contributed by the bonding states of the interaction between Mg atoms, Al atoms, and a small amount of Si atoms. Below the Fermi surface, the valence band in the range of 2-6 eV was mainly contributed by the *d*-state valence electrons of Cu atoms, and a small part was contributed by the *s*-state electrons of Al and Mg. For the lowest energy band part farthest from the Fermi surface, it was mainly the contribution of the *s*-state electrons of Si atoms and the mixing of s-state electrons of Mg and Al.

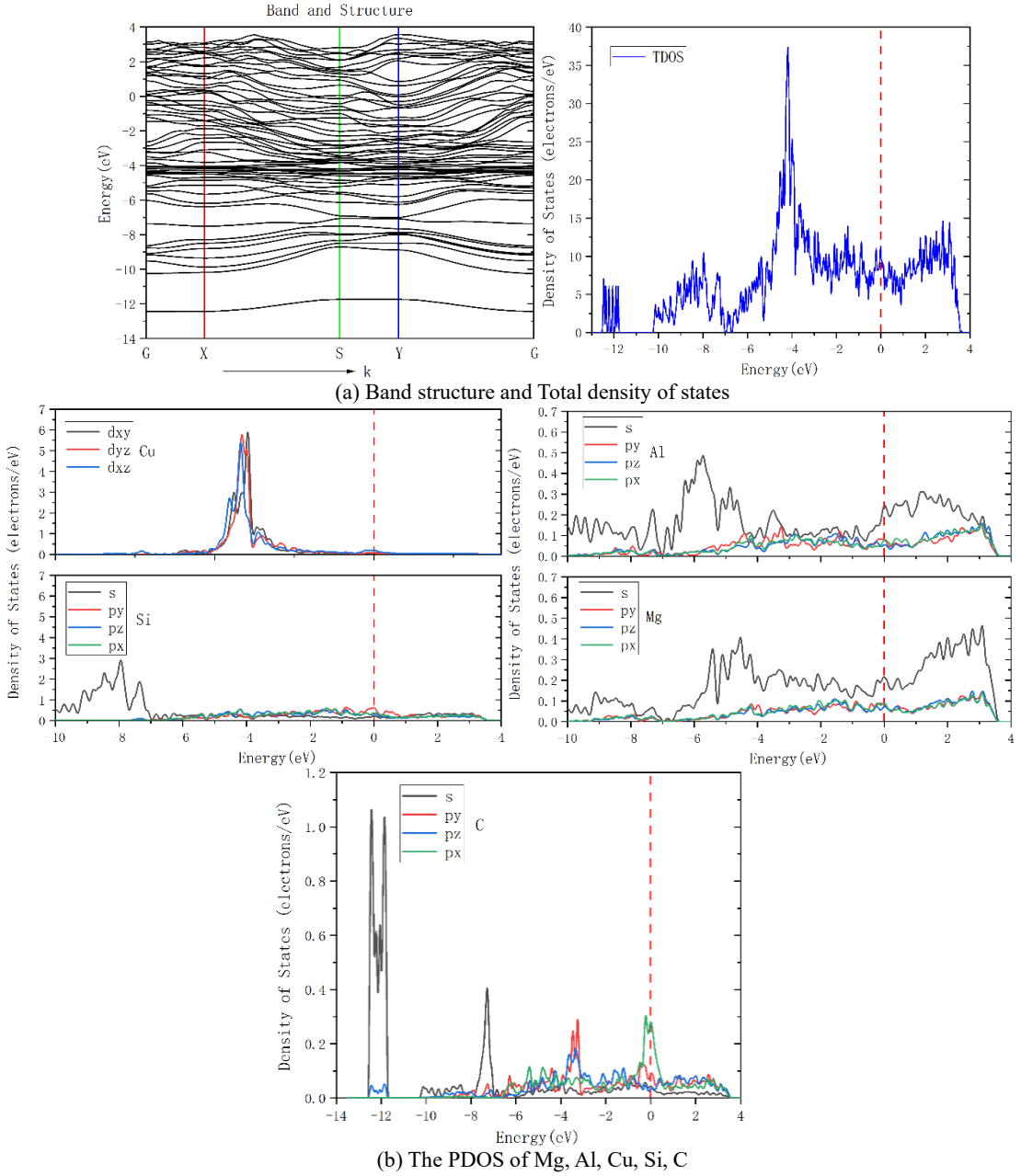

(a) Band structure and Total density of states

(b) The PDOS of Mg, Al, Cu, Si, C

Fig. 5. Electronic structure of model with C atoms added

Analysis of the electronic structure of the system after adding carbon atoms as shown in Fig. 5. It showed that the valence electron orbits of each atom had changed. As shown in Fig. 5-b, the PDOS values of Cu and Mg atoms increased at the main contributing energy levels, while the PDOS values of Al and Si atoms decreased. Compared with the non-added C atom, the energy band of the system after adding C moves slightly downward and tends to be more gentle. The peak increase of the total density of states in Fig. 5-a. became sharper, and a new isolated energy band in the -12.5eV valence band region can be saw and its density of states peaks were mainly contributed by the *s*-orbital valence electrons of C atoms. In addition, the value increase of the density of states at -7.2 eV was no longer 0, which was the contribution of the C-2*s* electronic state participation. The co-aggregation of the C-2*p* electronic state and the *s*-state electrons of Al, Mg, and Si, increased the DOS value at the Fermi level and the electron density value of the architecture.

After the addition of C atoms, the whole system has a synergistic effect, which made the extranuclear electrons localized. Although the localized C-2*s* electronic state increases the energy level broadening peak, and the free electrons near the C atom appear weakly localized, it did not affect the formation of the system and the stability of the structure [33]. Because the bonding state of each atom in the system changed after the addition of C atoms, due to the enhanced structural localization of electrons, the bonding between Mg, Al, Si, and Cu became weak. From the perspective of the partial density of states (PDOS), the *s* orbital (localized electron) of the C atom has a relatively strong DOS value relative to the *p* orbital in the valence band region, and in the conduction band region, the *p* orbital (delocalized electron) played a dominant role in the DOS.

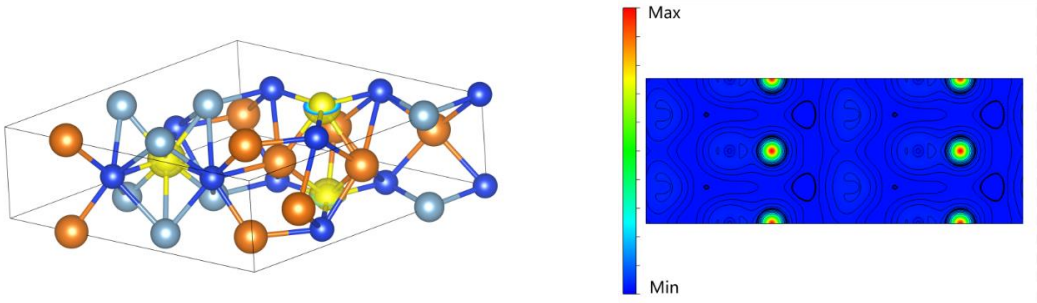

(a) Three-dimensional distribution (b) Two-dimensional (0 0 1) plane distribution surface

Fig. 6. Charge density

The charge density can intuitively show the transfer of charges after the atoms were bonded, and further analyze the charge density. As shown in Fig. 6-a, the charge transfer mainly occurs at the Cu atom from the analysis of the charge population, it can be intuitively seen from the charge density that the electrons around the Cu atom were symmetrical and spherically distributed. In this paper, the charge density of the (0 0 1) surface was calculated as shown in Fig. 6-b. The blue below the scale in the figure represents 0 electrons, and the electrons were gradually enriched upwards. However, there was a symmetrical electron loss and enrichment distribution near the Cu atom [34]. The missing electrons were the *d* orbital electrons of the Cu atom, and the electrons in the enriched area were the *p* orbital electrons of the Cu atom, and the electron distribution was spatially directional. Therefore, it was easy to form covalent bonds around Cu atoms. For example, the Al-Cu phase precipitated in a solid solution had obvious covalent bond characteristics [35, 36]. In the model, the number of electrons in the *d* orbital of the Cu atom varied greatly, and the delocalization of the 4*d* orbital electrons was very strong to form bonds with the hybridization of the surrounding atomic orbitals. It showed that the Cu element can be well integrated into the aluminum matrix composite material, which improves the structural stability of the material [37].

3.2. Mechanical Properties Results of Heat Treatment Orthogonal Experiments

To test the mechanical properties of the material after different heat treatments, it was decided to measure its mechanical properties by testing tensile strength, hardness, and elongation. Table 3 showed the heat treatment process scheme of this orthogonal experiment and the three mechanical properties of the tested samples under each heat treatment process. Three samples were taken from each heat treatment process for mechanical property testing to reduce the error caused by the experiment.

Table 4 was the average range analysis table of material properties under this orthogonal experiment. It can be seen from the table that for the tensile strength of composite materials, the solution time had the greatest impact, followed by the aging time and the solution temperature, and the aging temperature had the least effect on the tensile strength of the material. Moreover, the effect of solution temperature and aging time on the tensile strength of the material was almost the same, and the extreme difference was only 0.06. For the hardness of the composite material, its influence degree from large to small was the solid solution time, aging temperature, aging time, and solid solution temperature, and the influence degree of the solid solution time was more prominent than that of the other three process parameters. For the elongation of the material, the four process parameters had almost the same degree of influence. The most influential was the aging time, and the smallest was the aging temperature. The effect of solution treatment on the elongation of the material was moderate.

Table 3.
Orthogonal experiment table and experiment results

Experiment group number	Heat treatment process	Strength Rm (MPa)			Hardness H (HBS)			Elongation Δ (%)		
		Rm_1	Rm_2	Rm_3	H_1	H_2	H_3	Δ_1	Δ_2	Δ_3
1	$A_1B_1C_1D_1$	319.75	322.71	325.67	76.45	77.02	77.59	1.8	2.25	2.71
2	$A_1B_2C_2D_2$	352.75	356.25	349.25	77.06	78.18	75.93	2.15	1.37	2.91
3	$A_1B_3C_3D_3$	341.75	348.38	355	70.04	73.49	76.94	3.48	2.61	1.76
4	$A_2B_1C_2D_3$	356	358.25	353.75	79.10	81.38	76.82	2.91	1.23	2.07
5	$A_2B_2C_3D_1$	360.25	345.25	352.75	87.19	74.65	80.92	1.89	2.75	3.6
6	$A_2B_3C_1D_2$	345.25	349.75	340.75	70.10	73.28	66.92	2.92	1.35	2.13
7	$A_3B_1C_3D_2$	304.5	322.75	341	69.53	79.39	89.25	1.6	1.63	1.65
8	$A_3B_2C_1D_3$	351.25	345.5	357	80.19	76.88	83.50	1.29	1.25	1.33
9	$A_3B_3C_2D_1$	352	343	334	80.25	73.52	66.79	2.52	2.76	3.01

Table 4.
The average range of strength (MPa), hardness (HBS), elongation (%)

Mean value	A- Solution temperature	B- Solution time	C- Aging temperature	D- Aging time
Mean value k_1	341.28 MPa 75.86 HBS 2.34%	333.82 MPa 78.5 HBS 1.98%	339.74 MPa 75.77 HBS 1.89%	339.49 MPa 77.15 HBS 2.59%
Mean value k_2	351.33 MPa 76.71 HBS 2.32%	352.25 MPa 79.39 HBS 2.06%	350.58 MPa 76.56 HBS 2.33%	340.25 MPa 75.52 HBS 1.97%
Mean value k_3	339 MPa 77.7 HBS 1.89%	345.54 MPa 72.37 HBS 2.5%	341.29 MPa 77.93 HBS 2.33%	351.88 MPa 77.59 HBS 1.99%
Range R	12.33 MPa 1.84 HBS 0.45%	18.43 MPa 7.02 HBS 0.52%	10.26 MPa 2.16 HBS 0.44%	12.39 MPa 2.07 HBS 0.62%

Fig. 7 showed the influence curve of each heat treatment process parameter on the mechanical properties of the material. Under different heat treatment level parameters, the mechanical properties of composites had different variations. From Fig. 7, it was found that the $A_2B_2C_2D_3$ heat treatment scheme can achieve a higher strength of the composite. The heat treatment scheme of $A_3B_2C_3D_3$ can achieve a high hardness of the composite material. The heat treatment scheme of $A_1B_3C_2D_1$ or $A_1B_3C_3D_1$ can achieve a high elongation of composite materials. At the same time, it can be found that among the above three high-performance composite materials, the strongest materials experience a long solution and aging insulation time, up to 10 hours, the hardest materials experience a higher solution temperature, and the materials with the highest elongation experience the largest solution time.

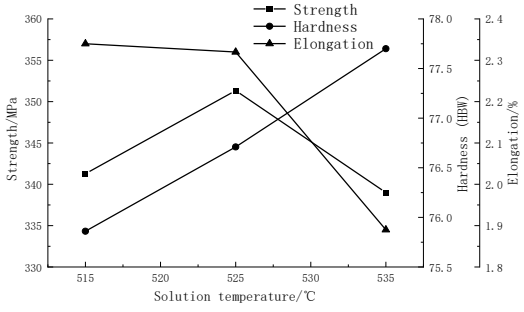

(a) Solution temperature

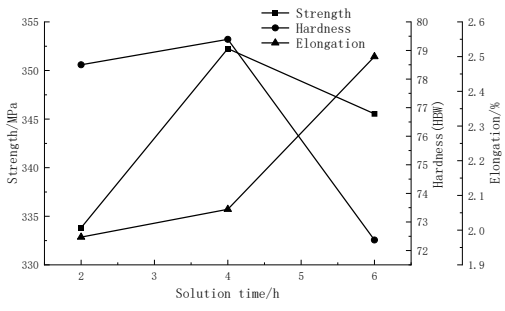

(b) Solution time

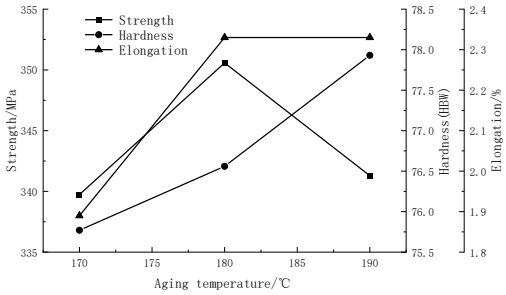

(c) Aging temperature

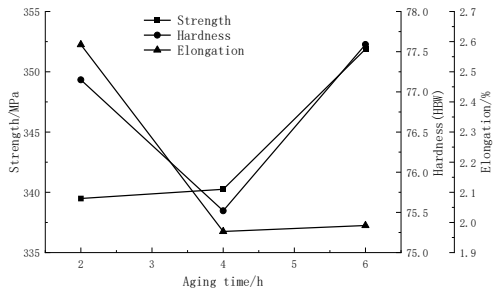

(d) Aging time

Fig. 7. Different heat treatment parameters for the mechanical properties of composites material

The effect of interactions on experimental results was not considered in this experiment. Table 5 was an ANOVA table for single-factor main effects detection in orthogonal experiments, which can accurately evaluate the degree of influence of each influencing factor on the experimental results [38]. The experimental results showed that the heat treatment process parameters had a light influence on the elongation of the composite, but have a significant effect on the strength of the material. Solution duration and aging time had the greatest influence on the strength of the composite, and the solution time had a significant impact on the hardness of the material, while the duration of solution had a greater impact on the elongation. After mechanical property testing, it was found that the carbon nanotube-reinforced ZL105 aluminum alloy specimen under the optimal solution time reached 376 MPa in strength and the hardness was 89.7 HBS and the elongation is 2.13%, which was greatly improved compared with the casting specimen (strength was 240 MPa, hardness was 69.55 HBS and the elongation was 1.72%).

Table 5.
Orthogonal test one-way analysis of variance table

Heat treatment factor	Sum of squares			Degrees of freedom	Mean square			*F* ratio			Significant *P*		
	1	2	3		1	2	3	1	2	3	1	2	3
A-Solution temperature	775.189	15.339	1.132	2	387.59	7.67	0.566	5.877	0.312	1.393	0.011	0.736	0.274
B-Solution time	1566.209	263	1.425	2	783.1	131.5	0.712	11.873	5.341	1.754	0.001	0.015	0.201
C-Aging temperature	619.184	21.574	1.138	2	309.59	10.787	0.569	4.694	0.438	1.402	0.023	0.652	0.272
D-Aging time	867.662	21.579	2.219	2	433.83	10.79	1.11	6.578	0.438	2.732	0.007	0.652	0.092
Error	1187.179	443.17	7.309	18	65.954	24.621	0.406						

1 - Strength Rm, 2 - Hardness HB, 3 - Elongation△

3.3. Microscopic Morphology Results

Fig. 8-a was the metallographic diagram of the best strength specimen (sample 32) in this experiment, after heat treatment ($A_2B_2C_2D_3$), the metallographic structure of the specimen is relatively delicate, and the grains are closely connected, and only some grain boundaries have slight segregation. Fig. 8-b was the metallographic diagram of the best hardness specimen (sample 36) in this experiment, after experiencing a high solid solution and aging temperature ($A_3B_2C_3D_3$), the strengthened phase is solidified again in the form of a linear or round sheet and tightly gathered on the grain boundary. Fig. 8-c was a metallographic diagram of the sample with the best elongation in this experiment (sample 38), after experiencing a high solution duration and aging temperature ($A_1B_3C_3D_1$), the metallographic structure is uniformly distributed, forming a dense network structure, and irregular black short rod-like reinforced phase uniformly precipitated on the grid-like grain boundaries.

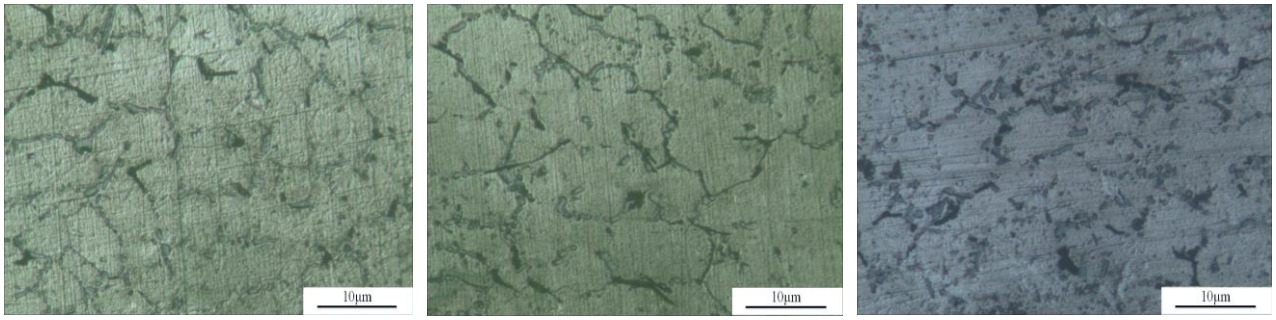

(a) Sample 32 (maximum strength) (b) Sample 36 (highest hardness) (c) Sample 38(the best elongation)

Fig. 8. Sample with the best mechanical properties after heat treatment

4. Analysis and Discussion

The experimental results showed that the incorporation of CNTs led to the improvement of the mechanical properties of the composites. In this section, the simulation calculations are combined with the experimental results to explore the mechanism of the mechanical properties of the composite with added CNTs affected by heat treatment.

4.1. Strength

During the loading process of the material, the internal structure of the material will deform. The heat-treated sample 32 was subjected to a tensile test, and its fracture form was found to be different from the typical brittle fracture in the fracture topography. There were planes bumpers at the bottom of the fracture morphology and a large number of dimples and microcracks. At the same time, it was observed the dimples was smooth and flat under in the enlarged view of the fracture morphology, while the shape of cross-sectional was sharp, as shown in Fig. 9.

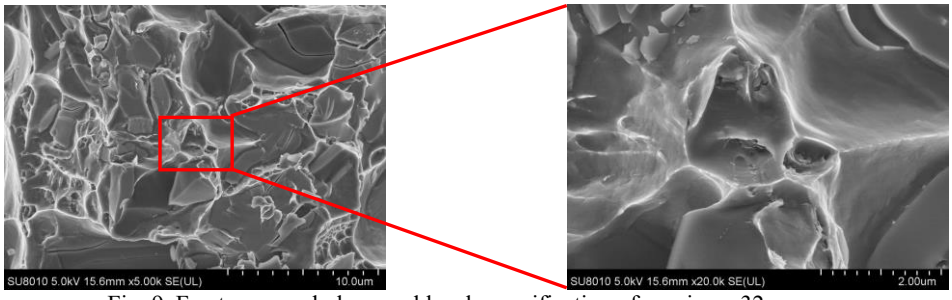

Fig. 9. Fracture morphology and local magnification of specimen 32

Firstly, the formation of this morphology was resulted by the addition of CNTs, which can causes numerous microscopic interfaces to be formed in the melt of the alloy. These microscopic interfaces were nucleation spots during preferential formation. In the nucleation process, the nanoparticles were accumulated, which can enforce the strength when the material is stretched and formed a platform on the bottom. The distribution without nanoparticle enhancement were torn and elongated by forces, forming sharp shapes around them.

Secondly, according to the PDOS diagram of each atom in Fig. 5-b, it was found that the C atomic level (0 eV, -3.5 eV, and -7.5 eV) participated the valence electrons of main elements (except Cu), which means that the compounds and second phase particles formed by the aggregation of C element with Mg, Al, and Si at the grain boundary. Based on the cell model and dot matrix parameters in Fig. 2, it was inferred that the crystal structure of the alloy is monoclinic. C atoms addition would increase the bonding force between the dense row surface and the dense row direction between the cells, which can significantly change the electronic structure at the grain boundaries. It can make the alloy lattice closer and stronger, which was increased strengthens of alloy.

In addition, CNTs have precise dimensions and extremely high strength. It could be stacked and slide during cast molding. When piece was heat treatment, the stress of solution precipitation and grain boundary slippage would increase. But the CNTs is highly flexible can overcome stress and strain of local area, and an elastic barrier was built in the alloy for resisting external forces. The process is shown in Fig. 10. This mechanism can effectively "elasticize" the weak defects caused by heat treatment, so that the large stress in the alloy was no longer concentrated in one position, but transmitted to the area close to CNTs. It would be reduced the stress at the loading point and make the grain obtain a large amount of elastic expansion. As a result, the tensile strength and breaking strength of the alloy were improved, the elongation of the material was also enhanced.

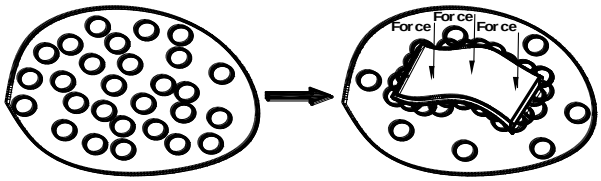

Fig. 10.The process of formation of an elastic barrier

4.2. Hardness

Fig. 11-a is the cast state and heat treated states (sample 36) after metallographic grinding and polishing corrosion. It showed that the cast state specimen consisted of hollow, coarse dendrites and eutectic silicon in the shape of a fish bone [39], and with a large structurally missing portion in the middle of the metallographic organization. There is no structural dense grain boundary as a connecting link, but wide and long sparse grain boundaries. So it cannot effectively transfer large loads from inside and outside, which led to the low hardness of the specimen.

Fig. 11-b showed the metallographic diagram of the material after $A_3B_2C_3D_3$ heat treatment. The metallographic organization was uniformly distributed, and numerous strengthening phases precipitate to the grain boundaries, forming a stable structure. Because the solid solution temperature provided the driving force for phase transformation during heat treatment, which can precipitate and refine the reinforcing phases [40]. Supersaturated solid solution inside the material can be obtained by solution treatment, and the hardness of the composite material can be improved by aging precipitation strengthening. In addition, a small circular GP zone and needle β-phase can be observed in the metallographic organization. The GP zone is co-ligated with the matrix and the β-phase is locally co-ligated with the matrix, both of which can prevent dislocations occurring to increase the material strength and hardness [41].

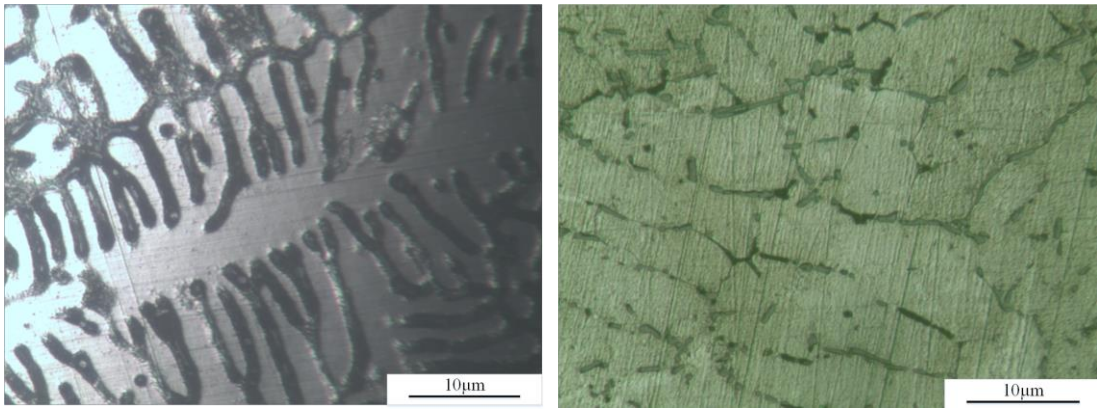

(a) Cast state (b) Heat treatment state ($A_3B_2C_3D_3$)

Fig. 11. Metallographic diagram of cast and heat-treated state (specimen 36)

From the atomic level, because of the orbitals of C atoms is sp^2, they would form C-Al covalent bonds with the shared electron pairs of Al. The internal structure of the material would consist of strongly bonded compounds of aluminum carbide [42], and the hardness of the composites was enhanced. Combined with the PDOS diagram of the C atom in the electronic structure Fig. 5-b, it was found that the energy state at the *s*-orbital valence electron contribution of the C atom was densely distributed. It indicates that the 2*s* state electrons of the C atom in the carbon nanotube enhancer cause an increase in the local valence electron concentration near the crystal defects when interacting with the Cu and Mg atoms in the aluminum matrix. This also caused an increase in the PDOS values of Cu and Mg atoms in Fig. 5-b. After heat treatment of the alloy, the C atoms made an ordered arrangement at the crystal defects, which makes the atoms fused in the solid solution structure undergo lattice distortion and eases the close contact of the solid solution tissues with each other. The distorted lattice affects the dislocation movement and prevents the grains from undergoing slip, thus increasing the hardness of the alloy solid solution [43].

4.3. Elongation

Fig. 12 is the TEM of specimen 38. The uniform dispersion of CNTs was the key to the performance of the enhanced composites [44]. A good internal interfacial bonding with uniform distribution of C atoms was observed on the Fig.12. The energy spectrum was shown in Fig.12-c. Comparing the results of the composition surface scan, it was found that there were many O elements on this region. It may be absorbed during the alloy melted at high temperature. After the CNTs were added, and it was easily to resolve the O_2 inhaled by the matrix material into the composite [45], and forming the C-O phase. The molecular bonds between CO_2 elements were prone to break at high temperatures, and

generating stable and adsorptive carbon bonds such as >C=O and >C=C=O on the carbon surface [46]. Thus, when the alloy was heat treated, the adsorbed moiety played a key role in the connection of the internal interface of the composite. The elongation of the composite was also improved and the toughness of the material was strengthened.

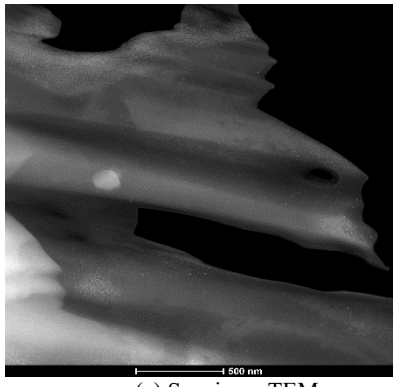

(a) Specimen TEM

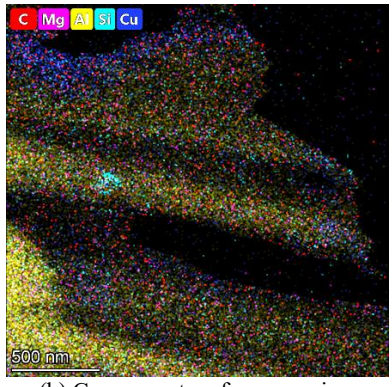

(b) Component surface scanning

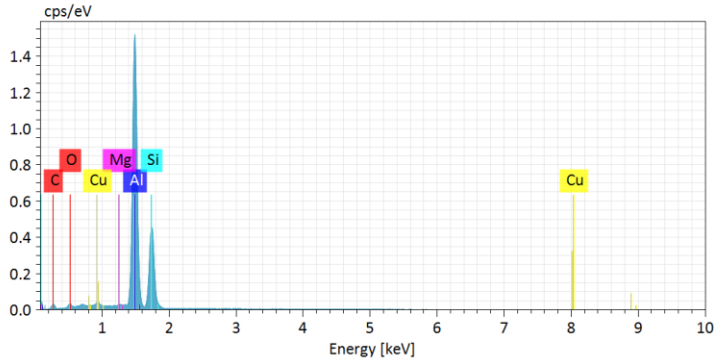

(c) Energy spectrum

Fig. 12. TEM and energy spectrum of specimen 38

5. Conclusions

Based on the simulation calculation of carbon atom added into aluminum alloy system and the optimization of the heat treatment process of cast aluminum alloy (ZL105) with CNTs, the following conclusions are obtained.

1. The atomic structure simulation shows that the atoms of various elements added to the aluminum matrix composite (ZL105) can form common electron pairs and strong bond compounds, which enhances the bonding ability between atoms in the metal. Although the addition of C atom changed the bonding state between atoms, but the affection for the forming and structural stability of the alloy system is light. And the strong bond compounds formed by C atoms and other elements inside the solid solution structure can significantly effect the material properties.
2. The key influencing factors of heat treatment for ZL105 alloy with CNTs was the solution time, while the aging time has the greatest influence for elongation. The solution time of 4 hours can balance the performance and cost of material heat treatment process.

Atomic simulation provides microscopic solutions for material enhancement mechanisms, but how to connect micro structure with macro performance also need more research, especially for casting engineering with the process of high energy atoms to castings.

Acknowledgments

This research was financially supported by the Industrial Research Projects of Guizhou Province, China (GZ NO.[2015]3004). Moreover, this research was also financially supported by the Guizhou Industry Simulation Design & Innovation Center (QKZYD NO.[2016]4006). This research was also supported by Guizhou Education Department Science and Technology Research Project Serve for the “Four new” and “Four modernizations” (QJJ [2022] No. 005). This research was also supported by Doctoral Research Foundation of Guizhou Normal University (2017). In the end, thanks the company of Guizhou Huaheng Machinery Manufacturing Co., Ltd. for their helping.

References

[1] Okayasu, M., Wu, S. & Hasanah, I.U. (2022). Effect of carbon nanotubes on the mechanical properties of cast Al–Si–Cu alloys. *Materials Science and Technology* 38(4), 237-245. https://doi.org/10.1080/02670836.2022.2037058.

[2] Hassanzadeh-Aghdam, M.K., Ansari, R. & Mahmoodi, M.J. (2018). Thermal expanding behavior of carbon nanotube-reinforced metal matrix nanocomposites-A micromechanical modeling. *Journal of Alloys and Compounds* 744, 637-650. https://doi.org/10.1016/j.jallcom.2018.02.100.

[3] Okayasu, M., Sahara, N. & Mayama, N. (2022). Effect of the microstructural characteristics of die-cast ADC12 alloy controlled by Na and Cu on the mechanical properties of the alloy. *Materials Science and Engineering*: A. 831, 142120. https://doi.org/10.1016/j.msea.2021.142120.

[4] Rodrigues, F.A.d.S., Paraguassu, W., Simões Vieira, S., M.F.G., Souza, J.A.d.S., Braga, E.d.M. & Reis, M.A.L.d. (2017). Electrical and tensile properties of carbon nanotubes-reinforced aluminum alloy 6101 wire. *Journal of Nanoscience and Nanotechnology.* 17(7) 4837-4841. https://doi.org/10.1166/jnn.2017.13429.

[5] Dobrzański, L.A., Tański, T. & Trzaska, J. (2010). Optimization of heat treatment conditions of magnesium cast alloys. *Materials Science Forum.* 638-642, 1488-1493. DOI:10.4028/www.scientific.net/MSF.638-642.1488.

[6] Li, R.X., Li, C.X. & Li, R.D. (2006). Study on the best heat treatment process of casting Al-Si-Cu-Mg alloy. *Casting.* (10), 1015-1019.

[7] Li, B., Wang, X., Chen, H., Hu, J., Huang, C. & Gou, G. (2016). Influence of heat treatment on the strength and fracture toughness of 7N01 aluminum alloy. *Journal of Alloys and Compounds.* 678, 160-166. https://doi.org/10.1016/j.jallcom.2016.03.228.

[8] F. Saba, F., Sajjadi, S.A., Haddad-Sabzevar, M. & Zhang, F. (2017). Formation mechanism of nano titanium carbide on multi-walled carbon nanotube and influence of the nanocarbides on the load-bearing contribution of the nanotubes inner-walls in aluminum-matrix composites. *Carbon.* 115, 720-729. https://doi.org/10.1016/j.carbon.2017.01.062.

[9] S.H. Zhou, S.H. & Napolitano, R.E. (2010). Phase stability for the Cu–Zr system: First-principles, experiments and solution-based modeling. *Acta Materialia.* 58(6), 2186-2196. https://doi.org/10.1016/j.actamat.2009.12.004.

[10] Liu, H., Papadimitriou, I., Lin, F.X. & Llorca, J. (2019). Precipitation during high temperature aging of Al−Cu alloys: A multiscale analysis based on first principles calculations. *Acta Materialia.* 167, 121-135. https://doi.org/10.1016/j.actamat.2019.01.024.

[11] Zhang, W.P., Ma, M.L., Yuan, J.W., Shi, G.-l., Li, Y.-j., Li, X.-g. & Zhang, K. (2020). Microstructure and thermophysical properties of Mg_2Zn_xCu alloys, *Transactions of Nonferrous Metals Society of China* 30(7), 1803-1815. https://doi.org/10.1016/s1003-6326(20)65340-7.

[12] Stemper, L., Tunes, M.A., Dumitraschkewitz, P., Mendez-Martin, F., Tosone, R., Marchand, D., Curtin, W.A. Uggowitzer, P.J. & Pogatscher, S. (2021). Giant hardening response in AlMgZn(Cu) alloys. *Acta Materialia.* 206 https://doi.org/10.1016/j.actamat.2020.116617.

[13] Petrik, M., Razumov, I., Gornostyrev, Y., Naschetnikova, I. & Popov, A. (2022). Kinetics of ordering and decomposition in Ti-Al-X (X = Si, Zr) alloys: monte carlo modeling. *Materials (Basel).* 15(16). https://doi.org/10.3390/ma15165722.

[14] Wu, B., Xie, Z., Huang, J., Lin, J., Yang, Y., Jiang, L., Huang, J., Ye, G., Zhao, C., Yang, S. & Sa, B. (2018). Microstructures and thermodynamic properties of high-entropy alloys CoCrCuFeNi. *Intermetallics.* 93, 40-46. https://doi.org/10.1016/j.intermet.2017.10.018.

[15] Haryadi, D. & Rudianto, H. (2020). Study of first principles of Mg-Si binary systems as precipitates from T6 heat treatment of Al-Mg-Si alloys. *Indonesian Journal of Applied Physics.* 10(1), 16-23. https://doi.org/10.13057/ijap.v10i01.28912.

[16] Bhattacharyya, J.J., Wang, F., Stanford, N. & Agnew, S.R. (2018). Slip mode dependency of dislocation shearing and looping of precipitates in Mg alloy WE43. *Acta Materialia* 146, 55-62. https://doi.org/10.1016/j.actamat.2017.12.043.

[17] Li, M., Zhang, G., Yin, S., Wang, C., Fu, Y., Gu, C. & Guan, R. (2022). Transformation of long-period stacking ordered structures in Mg-Gd-Y-Zn alloys upon synergistic characterization of first-principles calculation and experiment and its effects on mechanical properties. *Journal of Magnesium and Alloys.* 3, 1-13. https://doi.org/10.1016/j.jma.2022.09.027.

[18] Zhao, Y., Li, H. & Huang, Y. (2021). The structure, mechanical, electronic and thermodynamic properties of bcc Zr-Nb alloy: A first principles study. *Journal of Alloys and Compounds.* 862, 158029. https://doi.org/10.1016/j.jallcom.2020.158029.

[19] Zhang, B., Fu, L., Ge, H., Rong, X., Xiong, K., He, J. & Mao, Y. (2022). Revealing the Origin of Heterogeneous Phase Transition and Deformation Behavior in Au-Ag-Cu-Based Multicomponent Alloys. *Metals.* 12(11), 1-17. https://doi.org/10.3390/met12111966.

[20] Fransson, E., Gren, M. & Wahnström, G. (2021). Complexions and grain growth retardation: First-principles modeling of phase boundaries in WC-Co cemented carbides at elevated temperatures. *Acta Materialia.* 216, 1-11. https://doi.org/10.1016/j.actamat.2021.117128

[21] G. Wang, G. & Li, X.M. (2020). First-principles calculation of the effects of Cu and Co content on CoCuFeNi high-entropy alloys. *Functional Materials.* 51(03), 3189-3195.

[22] Yu, J.Y., Wang, K.M. & Wang, Z.M. (2018). First-principles calculation of elastic properties of high-entropy alloy CoCrFeNi. *Journal of Liaoning University of Science and Technology.* 41(05), 357-361. https://doi.org/10.13988/j.ustl.2018.05.006.

[23] Lv, Z., Yao, J.P., Tang, J.Q. & Chen, Z.J. (2022). First-principles study of electronic structure at the interface of 3C-SiC/Mg composites. *Chinese Journal of Atomic and Molecular Physics interface.* 39(04), 157-162. https://doi.org/10.19855/j.1000-0364.2022.046007.

[24] Xiong, M.Y., Zhang, R., Wen, D.L. & Su, X. (2022). First-principles study on electronic structure and p-type characteristics of Ag-O co-doped GaN nanotubes. *Micro-Nano Electronics.* 59(05), 410-416. https://doi.org/10.13250/j.cnki.wndz.2022.05.004.

[25] Wang, L.X., Yao, S. & Wen, B. (2019). First-principles

calculation of the effect of Fe content on the AlFe_xTiCrZnCu mechanical properties of high entropy alloys. *Materials Reports.* 33(S2), 356-359.
[26] Deng, J. (2021). Design and first-principles calculation o f new magnetic semimetals and semiconductors[D]. *Univ ersity of Chinese Academy of Sciences (Institute of Phys ics, Chinese Academy of Sciences)*. https://doi.org/10.276 04/d.cnki.gwlys.2021.000057.
[27] Wang, V., Xu, N., Liu, J.C., Tang, G. & Geng, W.T. (2021). VASPKIT: A user-friendly interface facilitating high-throughput computing and analysis using VASP code. *Computer Physics Communications.* 267, 108033, 1-19. https://doi.org/10.1016/j.cpc.2021.108033.
[28] Kadioglu, Y., Üzengi Aktürk, O. & Tomak, M. (2014). Electronic and geometric structure of AuxCuy clusters st udied by density functional theory. *International Journal of Modern Physics.* C, 25(06), 1450011. https://doi.org/1 0.1142/s0129183114500119.
[29] Shao, G.J. (2009). Effect of addition of element Cu on precipitated phase behavior of Al-Mg-Si alloy. *Journal of Materials and Heat Treatment.* 30(03), 67-70.
[30] He, Z.W., Chen, J.B. & Yang, J.S. (2019). Structural co nstruction and performance of FeNiMnCu0.2Alx based o n first principles. *Journal of Wuhan University of Light Industry.* 38(04), 37-39+93. https://doi.org/10.3969/j.issn.2 095-7386.2019.04.008.
[31] Lan, Z.H., Hou, M.Y., Wang, H.Y. & Ji, Y.G. (2014). Analyzing of energy band and density of states of ZnO. *Applied Mechanics and Materials.* 492, 273-275. DOI:10.4028/www.scientific.net/AMM.492.273.
[32] Man, T.T., Shang, J., Feng, J.L., Zhang, J.G., Shu, Y.J., Zhang, T.L. & Zhou, Z.N. (2013). Theoretical study of amino, hydrazine, azidodisubstituted hogentetrazine. *Energetic Materials.* 21(03), 281-288.
[33] Wang, X.J., Wang, L.L., Huang, W.Q., Tang, L.M. & Chen, K.Q. (2006). Local electronic states and electron transport in multicomponent superlattices with structural defects under magnetic fields. *Acta Physica Sinica*. (07), 3649-3655.
[34] Nemla, F. & Cherrad, D. (2022). First principles study of structural, elastic, electronic, and optical properties of the cubic perovskites AVO3 (A = Ca and La). *Emergent Materials* 5(1), 175-186. https://doi.org/10.1007/s42247-022-00369-9.
[35] Chen, J., Yoshida, K., Suzudo, T., Shimada, Y., Inoue, K., Konno, T.J. & Nagai, Y. (2022). In situ TEM observation and MD simulation of frank partial dislocation climbing in Al–Cu alloy. *Materials Transactions.* 63(4), 468-474. https://doi.org/10.2320/matertrans.MT-M2021233.
[36] Ravi Narayan, L. & Hebert, R.J. (2022). Rheology of partially solidified hypoeutectic aluminum copper alloys. *SN Applied Sciences.* 4(186), 1-14. https://doi.org/10.1007/s42452-022-05070-4.
[37] Han, T. (2020). Effect of copper content on solidification characteristics of AI-Cu alloy. *Metallurgy and Materials* 40(05), 63-64.
[38] Luo, C., Liu, K., Shi, X.Q., Liang, X.B. & Zhang, J.W. (2020). Orthogonal test analysis of heat treatment process parameters of Ti-22Al-25Nb alloy. *Hot Working Process.* 49(16), 121-124. https://doi.org/10.14158/j.cnki.1001-3814.20200769.
[39] Yu, D.X., Hu, O.L. & Zeng, R.X. (2020). Effect of heat treatment process on microstructure and mechanical properties of low silicon Al-Si-Mg cast aluminum alloy. *Shanghai Metal.* 42(04), 66-71+77.
[40] Dai, X.Y., Xia, C.Q. & Liu, C.B. (2007). Effect of solution treatment and timeliness on microstructure and properties of 7xxx aluminum alloy. *Journal of Materials and Heat Treatment.* No.100(04), 59-63.
[41] Yu, W. (2020). Effect of aging time on microstructure and mechanical properties of automobile 6063 aluminum alloy. *Hot Working Technology.* 49(14), 134-136. https://doi.org/10.14158/j.cnki.1001-3814.20192766.
[42] Peng, K.W., Wu, W.Y., Xu, J.Y. & Tu, G.F. (2008). Chemical reactions and phase composition of B_4C and Al at high temperature. *Rare Metals and Cemented Carbide.* (01), 16-19+33.
[43] He, C. (2020). Lattice defects and their partial polymerization characteristics in Mg-Bi and Mg-Gd alloys. *Chongqing University*. DOI: 10.27670/d.cnki.gcqdu.2020.000035.
[44] Esawi, A.M.K., Morsi, K., Sayed, A., Taher, M. & Lanka, S. (2010). Effect of carbon nanotube (CNT) content on the mechanical properties of CNT-reinforced aluminium composites. *Composites Science and Technology.* 70(16) 2237-2241. https://doi.org/10.1016/j.compscitech.2010.05.004.
[45] Chen, M., Fan, G., Tan, Z., Yuan, C., Guo, Q., Xiong, D., Chen, M., Zheng, Q., Li, Z. & Zhang, D. (2019). Heat treatment behavior and strengthening mechanisms of CNT/6061Al composites fabricated by flake powder metallurgy. *Materials Characterization.* 153, 261-270. https://doi.org/10.1016/j.matchar.2019.05.017.
[46] Jin, J.M. (2000). Catalytic mechanism of carbonate in solid carburizing agent. *Metal Heat Treatment.* (10), 37-41. https://doi.org/10.13251/j.issn.0254-6051.2000.10.020.